Initial Measurements of Plume Impingement in the NASA Langley 60-foot Vacuum Sphere

Neil S. Rodrigues[1], Ashley M. Korzun[2], Casey J. Broslawski[3]
NASA Langley Research Center, Hampton, VA, 23681

Tal Schwartz[4], Edward J. Nemie[5]
AMA Inc. at the NASA Langley Research Center, Hampton, VA 23681

Wesley A. Chambers[6],
NASA Marshall Space Flight Center, Huntsville, AL

Robert L. Wagner[7],
STC Inc. at the NASA Langley Research Center, Hampton, VA 23681

Paul M. Danehy[8], Raymond T. Lueg[9], Michael Wilson[10], Justin Shafner[11], David Tucker [12], Lianne Kuster[13], Jonathan Crider[14], J. Dave Lehotay[15]
NASA Langley Research Center, Hampton, VA, 23681

Amanda M. Braun[16]
NASA Postdoctoral Program at the NASA Langley Research Center, Hampton, VA 23681

Miguel X. Diaz-Lopez[17]
Johns Hopkins University, Baltimore, MD, 21218

[1] Optical Physicist, Advanced Measurements and Data Systems Branch, AIAA Senior Member. Neil.S.Rodrigues@nasa.gov
[2] Aerospace Engineer, Atmospheric Flight and Entry Systems Branch, AIAA Associate Fellow.
[3] Research Aerospace Engineer, Aerothermodynamics Branch, AIAA Member.
[4] Research Scientist, Advanced Measurements and Data Systems Branch, AIAA Member.
[5] Principal Mechanical Engineer, Mechanical Systems Branch, AIAA Member.
[6] Physicist, Natural Environments Branch.
[7] Mechanical Engineer, Mechanical Systems Branch, AIAA Member.
[8] Senior Technologist, Advanced Measurements and Data Systems Branch, AIAA Associate Fellow.
[9] Aerospace Engineer, Electronic Systems Branch, AIAA Member.
[10] Aerospace Engineer, Electronic Systems Branch, AIAA Member.
[11] Research Aerospace Engineer, Atmospheric Flight and Entry Systems Branch, AIAA Member.
[12] Engineering Technician, Manufacturing Applications Branch.
[13] Facility Systems Safety Engineer, Aerosciences Operations Section.
[14] Engineering Technician, Aerosciences Operations Section.
[15] Project Manager, Space Technology & Exploration Program Analysis Office.
[16] Postdoctoral Fellow, Advanced Measurements and Data Systems Branch, AIAA Member.
[17] NSTGRO Graduate Fellow, Department of Mechanical Engineering, AIAA Member.

An initial characterization of a gaseous, non-combusting ethane plume impinging on a flat plate in the NASA Langley 60-foot vacuum sphere is reported in this work. The motivation for this study is to characterize plume-surface interaction at conditions relevant to large-scale lunar landers. The gas-phase nature of this work focuses on characterization of the supersonic plume impingement on a flat plate. Since this effort is primarily driven to verify that the expected plume flowfield is obtained prior to testing with lunar regolith simulant, this work can be viewed in the context of characterizing a new or modified test facility. As part of these efforts, laser-based measurements are reported for the first time in this large-scale, legacy NASA vacuum facility. Laser Rayleigh imaging, focusing on the region near the impingement plate, shows a clear stagnation shock and quantitative values are reported for the height and curvature of the shock with respect to the flat surface.

I. Nomenclature

D_e	=	nozzle exit diameter
h	=	height of nozzle exit relative to surface
M_e	=	nozzle exit Mach number
P_a	=	vacuum sphere ambient pressure
P_e	=	nozzle exit pressure
P_0	=	nozzle total pressure
PT	=	pressure transducer
Re_e	=	nozzle exit Reynolds number
T_a	=	vacuum sphere ambient temperature
T_e	=	nozzle exit temperature
T_0	=	nozzle total temperature
TC	=	thermocouple probe
γ	=	specific heat ratio

II. Introduction

In recent years, there has been a heightened interest in understanding the interaction between a rocket exhaust plume and the surface upon which it impinges during powered decent and landing on planetary bodies such as the Moon and Mars. This interest in plume-surface interaction (PSI) is driven by risks to the vehicle, potential payloads, and surface assets due to the rocket plume-induced erosion and ejecta. Improved understanding of PSI phenomena through ground test data is critical for revealing the sensitivities of relevant gas and granular physics to parameters such as rocket thrust, altitude, and ambient pressure. A recent review paper by Cuesta *et al.* [1] provides a comprehensive overview on PSI experimental efforts, including recent tests in large-scale vacuum chamber facilities conducted at NASA [2-8] and at several universities including Auburn University [9-14], the University of Glasgow [15-18], and the University of Illinois Urbana-Champaign [19-21].

A simplified gas-phase experimental configuration relevant to PSI is the impingement of a supersonic jet on a flat plate. This canonical problem was explored in a large-scale vacuum sphere during the Apollo era [22] and was recently investigated by Al-Rashdan *et al.* [23] and Subramanian *et al.* [24]. A large-scale ground test for plume impingement was also performed in a 20-foot vacuum chamber at NASA Marshall Space Flight Center using planar laser-induced fluorescence (PLIF), which is a molecular-based, 2D (two-dimensional) measurement technique that can be used to visualize the flow of a targeted atom or molecule [25-29]. Nitric oxide (NO) PLIF measurements of plume impingement were previously also performed by Inman *et al*. [30] to study supersonic jet impingement for a non-planetary-landing application. Studies in the literature typically characterize plume impingement behavior based on the exit pressure ratio P_e/P_a, which is the ratio of the plume exit pressure (P_e) to the ambient pressure (P_a). The exit pressure ratio defines the nozzle expansion condition. Another common parameter in the literature is the exit Reynolds number Re_e, which can be calculated using the expression:

$$Re_e = \frac{\left(\frac{P_e}{RT_e}\right)\left(M_e\sqrt{\gamma_e RT_e}\right)D_e}{\mu_e}. \tag{1}$$

In the above expression, R is the gas constant, T_e is the exit temperature, M_e is the exit Mach number, γ_e is the exit specific heat ratio, D_e is the exit diameter, and μ_e is the exit viscosity.

Plume impingement experiments in the literature often utilize cold or heated nitrogen as the test gas to reduce the experimental complexities associated with combustion. While fundamental fluid mechanical insights can be obtained using these scaled experiments, the specific heart ratio γ (also known as the isentropic exponent) differs for nitrogen ($\gamma = 1.4$) compared to combustion gas products ($\gamma \sim 1.2$). In recent years, NASA Technical Memorandum reports by Jones [31, 32] describe the potential of heated, non-combusting ethane for scaled plume studies to match the specific heat ratio of hot-fire rocket engines.

This paper provides a summary of initial measurements of plume impingement acquired at NASA Langley Research Center, where a gaseous, non-combusting ethane plume is expanded into a 60-foot vacuum sphere at a reduced ambient pressure of nominally $P_a = 100$ Pa. These experiments are motivated by the desire to acquire new PSI data to reduce risks inherent with landing vehicles of larger mass and engine thrust on the lunar surface. The test configuration presented in this paper features the plume impinging onto a flat plate instead of a bed of lunar regolith simulant. The gas-phase nature of this work, focusing on the characterization of the supersonic plume impingement, is performed to verify that the expected plume flowfield is obtained and to serve as validation data for numerical predictions of the plume impingement behavior. Laser Rayleigh scattering measurements are performed near the impingement plate surface to visualize the stagnation shock. More information on Rayleigh scattering can be found in the literature in references such as Miles *et al.* [33]. Rayleigh scattering was chosen for this experimental configuration due to the relatively high (~6x) Rayleigh cross-section of gaseous ethane compared to nitrogen [34]. Installation and shakedown of the laser Rayleigh scattering instrument marks the first-ever utilization of a laser diagnostic measurement system at this large-scale, legacy NASA vacuum facility, and serves as a valuable point of departure for future efforts involving more sophisticated diagnostics such as particle imaging velocimetry and planar laser-induced fluorescence.

III. Experimental Systems

A. Vacuum Sphere Facility

The NASA Langley 60-foot vacuum sphere, which is located within the Langley Aerothermodynamics Laboratory (LAL), primarily utilizes a steam ejector to create a reduced pressure environment. The 60-foot vacuum sphere was previously used as a space environment simulator to conduct PSI testing for Apollo in the 1960s [35] and Viking in the 1970s [36] Both the steam ejector and the vacuum sphere are critical infrastructure for the LAL 31-inch Mach 10 tunnel, as shown in Fig. 1. Two different pressure transducers (PTs) located near the test hardware at the bottom of the vacuum sphere were used to measure the ambient pressure. A 0-15 psia Omega® pressure transducer (P/N PX309-015AI) was used to monitor the pressure for the majority of the vacuum pump-down operations in the sphere. A 0-10 Torr MKS Baratron® (P/N 626D11TDE) was activated once the sphere was within the range of the transducer and was the primary instrument for pressure measurement before, during, and after plume measurements. Once the sphere reached a sufficiently low pressure, and prior to testing with the plume, the steam ejector was isolated, and a positive displacement blower was activated to reach a lower ambient pressure typically near 100 Pa. The ambient temperature was monitored using a Type-K thermocouple (TC) probe. Ambient pressure and temperature measurements were sampled at 100 Hz during pump-down and 5000 Hz during plume testing using a Keyence® NR-X Multi Input Data Logger. A summary of the vacuum sphere instrumentation is shown in Table 1. The raised platform at the bottom of the vacuum sphere supports the majority of the test article hardware discussed in the next section.

B. Test Article

A pressure system enabling the flow of heated ethane through a converging-diverging nozzle was installed at the test facility. The system, adapted from the one reported in Ref. 30, consisted of an ethane cylinder, two nitrogen gas cylinders, an ethane piston tank, electrical heaters, regulators, and valves. The majority of the system was located outside of the sphere, with the flow of ethane directed into the sphere through a feedthrough flange. Ethane was isolated outside of the sphere until the test run auto-sequence was activated.

The test article primarily consisted of a supersonic nozzle and a 1.2-m diameter flat impingement plate that was oriented perpendicularly to the nozzle flow. The supersonic nozzle featured a nozzle exit-to-throat area ratio $A_e/A_t = 10$ and a nozzle exit diameter $D_e = 1.71$ cm, designed specifically to produce a highly underexpanded plume. The supersonic nozzle and associated fluid components were located on a panel allowing the nozzle height to be discretely varied between runs. The impingement plate, which was painted black to minimize geometric scattering from the laser, consisted of an outer plate and an inner plate. Sensors, including those to measure surface pressure and wall shear, were installed on the inner plate; these sensors and data from them are not discussed further in this paper. For the data presented in this paper, the nozzle height was fixed to 13.68 cm above the plate, resulting in a dimensionless height with respect to the nozzle exit diameter of $h/D_e = 8$. Ethane flow during test runs occurred for approximately

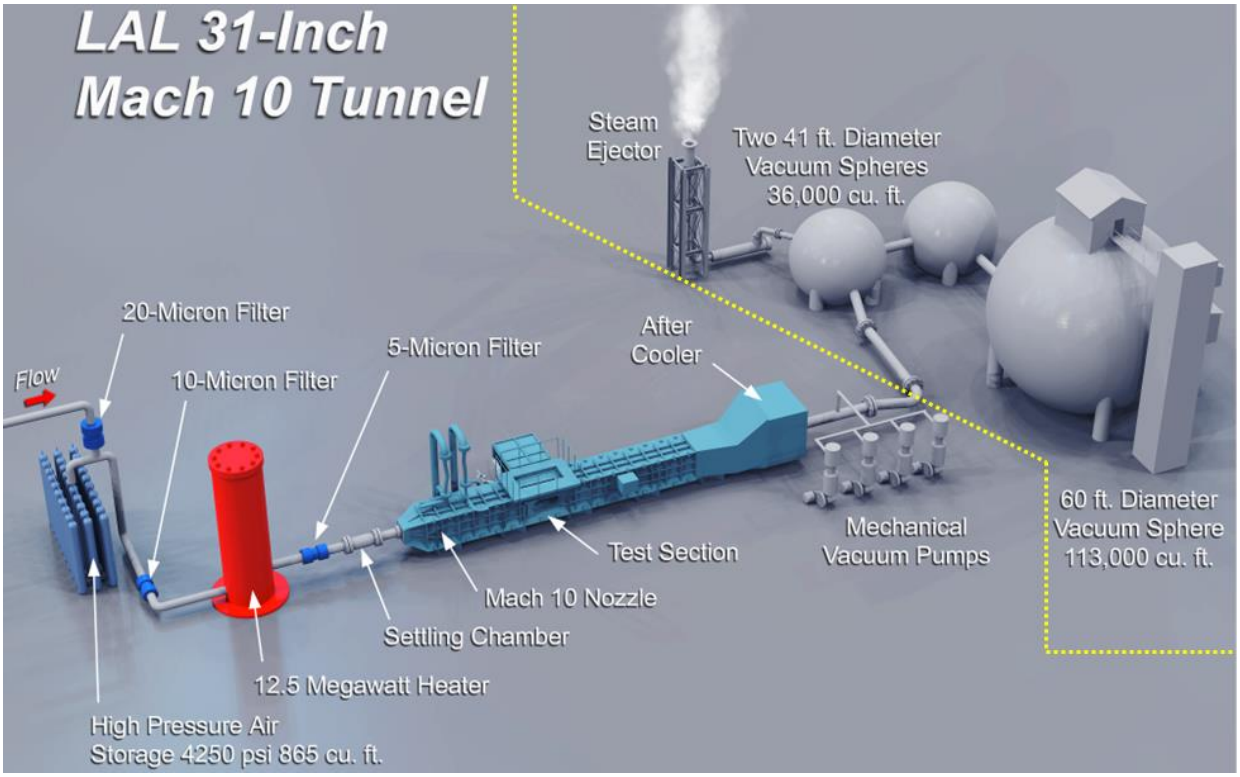


Fig. 1. 3-D schematic of the Langley Aerothermodynamics Laboratory (LAL) featuring the 60-foot Vacuum Sphere, 31-inch Mach 10 Tunnel, and associated critical infrastructure.

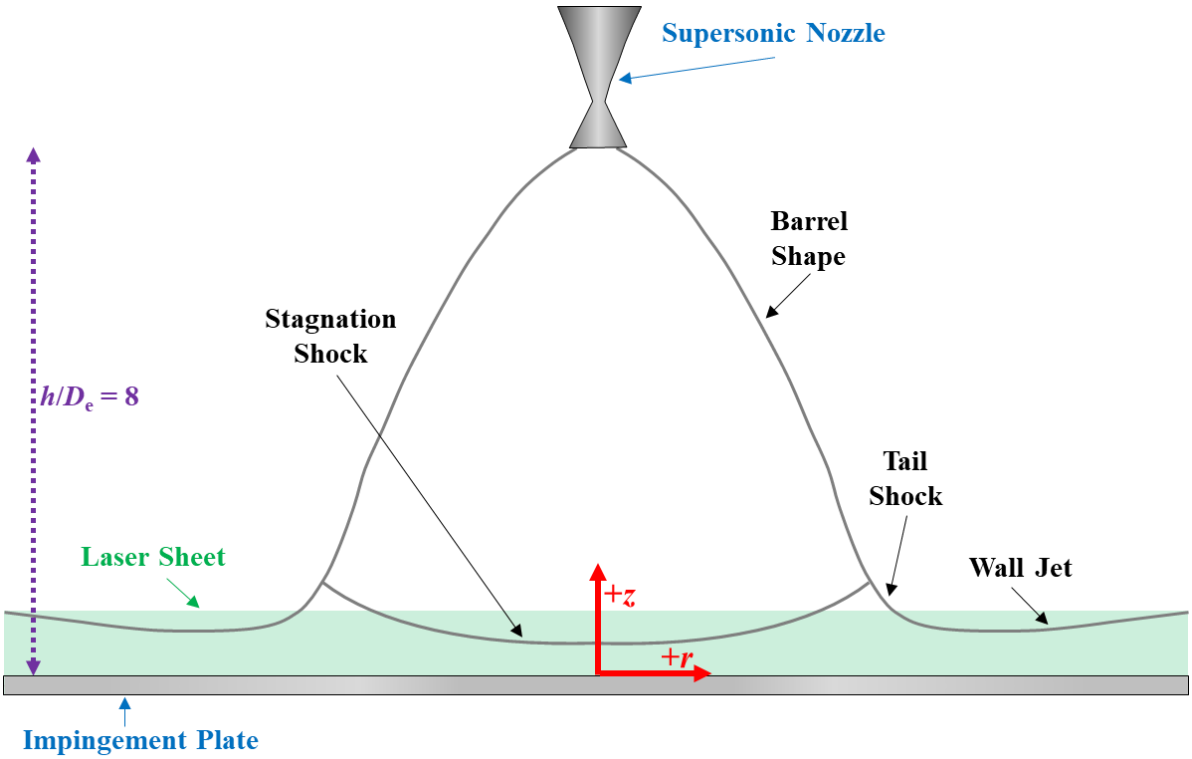


Fig. 2. Annotated diagram of the plume impingement apparatus showing the supersonic nozzle, impingement plate, laser sheet, and representative flow features. Also shown is the coordinate system for the present work.

Measurement	Instrument	Range	Uncertainty
Ambient Pressure, P_a	Sphere High PT	103.4 [kPa]	0.3 [kPa]
	Sphere Low PT	0 – 1.33 [kPa]	0.25% reading
Ambient Temperature, T_a	Sphere TC	273 – 373 [K], > 373 [K]	2.2 [K], 0.75% reading
Jet Stagnation Pressure	Nozzle PT #1	0 – 20684.3 [kPa]	8.3 [kPa]
	Nozzle PT #2		
Jet Stagnation Temperature	Nozzle TC #1	273 – 373 [K], > 373 [K]	2.2 [K], 0.75% reading
	Nozzle TC #2		

Table 1. Range and uncertainty for the vacuum chamber and nozzle instrumentation.

6 seconds between opening and closing of a remotely controlled pneumatic run valve, which was located upstream of the instrumented nozzle plenum. The nozzle plenum featured two GE® UNIK50E6 pressure transducers and two K-type thermocouple probes. The plume stagnation pressure and temperature were sampled at 100 Hz using a National Instruments® data acquisition system. A summary of the nozzle instrumentation range and uncertainty is also shown in Table 1. A schematic of the test article (supersonic nozzle and impingement plate) and expected plume impingement behavior is shown in Fig. 2. Also shown in Fig. 2 is the laser sheet for the Laser Rayleigh Scattering measurements.

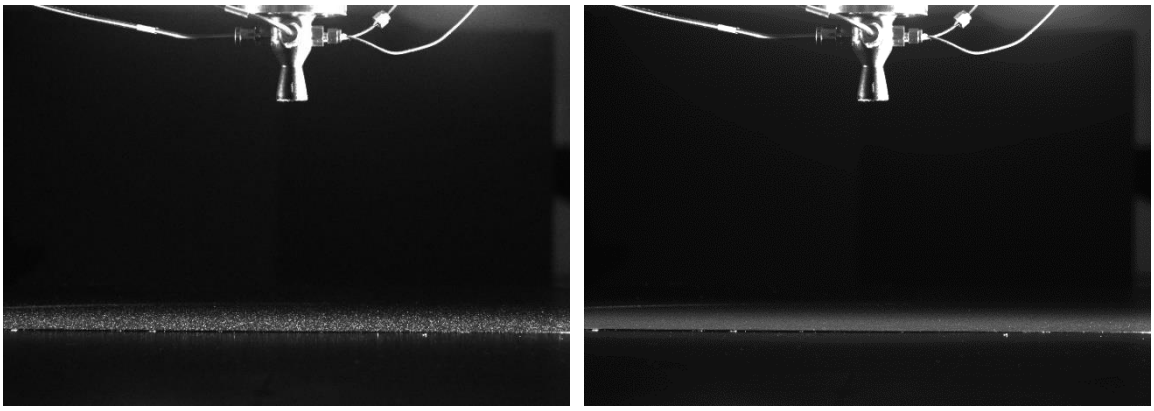
C. Laser Rayleigh Scattering System

Planar laser Rayleigh scattering of the ethane plume was enabled using a Quantel® Evergreen 200 Nd:YAG laser at 532 nm. The laser features two separately controlled laser heads (with distinct flashlamps and Q-switches) within the laser unit. The laser was operated at a repetition rate of 10 Hz, with the time delay between the pair of 10 ns laser pulses set to 40 ns to maximize instantaneous power. Operating the laser in this manner enabled a short enough time duration to effectively freeze the dynamics of the plume between the pulses, but with a long enough separation time to reduce the likelihood of damage to the laser passthrough window and associated optics. The laser system was installed in a room located adjacent to the vacuum sphere at its equator. Rayleigh scattering from gas molecules is optimized when the polarization is parallel to the image plane, whereas Mie and geometric scattering from particles and surfaces are comparatively insensitive to the laser polarization. Therefore, a half-wave plate was installed near the laser exit to optimize the polarization and ensure near-optimal Rayleigh scattering signal at the test article.

Following reflections off two dichroic mirrors, the laser was directed through a telescope consisting of spherical -50 mm and +200 mm focal length lenses. These lenses were used to expand and collimate the laser beam to a roughly circular beam of approximately 20 mm in diameter. The telescope system was crucial to maintain the quality of the laser given the long propagation distance to the test article of approximately 20 meters. Following another reflection off a dichroic mirror, the laser beam was directed to a periscope in order to pass the laser beam through a window and into the sphere. The window assembly consisted of a BK7 glass window installed in a 6-inch Conflat flange. A custom flange was installed to adapt the Conflat flange to the existing bolt pattern on the 60-foot sphere wall. The dichroic mirror immediately before the window was installed on a Newport® Picomotor mirror mount, enabling remote control of the tuning axes. A Thorlabs® laser shutter was used immediately before the last mirror in the room to permit the laser beam to pass through the glass window only when desired.

Upon passing through the window, the laser beam was directed to an in-sphere optical system located on a custom structure at the floor of the vacuum sphere. For the present work, this optical system consisted of three dichroic mirrors and a +2500 mm cylindrical lens. The three mirrors, each located on a vacuum-compatible Picomotor mirror mount, were used to direct the laser towards the test article. The cylindrical lens was used to focus the approximately 20 mm diameter laser beam into a vertical laser sheet, with the focus of the lens near the centerline of the nozzle. The laser sheet was located near the surface of the impingement plate and was terminated after traversing across the test article by a beam block. The two nearly simultaneous laser pulses were measured to be approximately 430 mJ per pulse pair at the laser exit and approximately 280 mJ at the test article.

Rayleigh scattering was collected approximately 90 degrees from the laser propagation direction using a greyscale Teledyne® Blackfly S camera (P/N BFS-PGE-50S4M-X), which is a GigE machine vision CMOS camera. The primary motivation for using this camera was due to the ability of NASA Langley engineers to harden the camera for vacuum operation, obviating the need for a dedicated camera enclosure. The camera was equipped with a 25 mm focal length, *f*/1.8 camera lens and a 532 nm bandpass filter. The camera was operated with a bit depth of 16 and with



(a) **(b)**

Fig. 3. (a) Instantaneous and (b) time-averaged laser scattering images at atmospheric pressure. The images show both Rayleigh scattering (gas phase) and geometric scattering from particles and surfaces.

a cropped sensor to accommodate operation at a 10 Hz repetition rate, synchronized to the laser system. The cropped sensor featured a pixel resolution of 2048 [H] x 1448 [V] pixels (pixel size is 2.74 μm) and the camera was operated with an A/D gain of 10. The camera was located roughly 2 meters from the plane of the laser sheet, resulting in an approximate magnification of 0.16 mm/pixel. Spatial calibration was performed using a calibration target with custom dot spacing and an in-house dewarping code. An instantaneous and a time-averaged (over 10 seconds) Rayleigh scattering image at atmospheric pressure are shown in Fig. 3. The images were obtained prior to any vacuum sphere or plume operations and are shown with sensor dark noise background subtracted. Dust particles in the sphere can be clearly seen while the weaker Rayleigh signal from air can be seen in the region between dust particles. A second vacuum-hardened Teledyne Blackfly S camera was also positioned inside the vacuum sphere to monitor the laser sheet during vacuum sphere operations and potentially correct for misalignment during pump-down. Although not performed for the present work, the second camera was oriented to potentially correct the Rayleigh scattering images from the primary camera during the test run for the laser sheet intensity variation and for pulse-to-pulse energy fluctuations.

IV. Results and Discussion

A. Representative Vacuum Sphere Pump-Down

A representative facility pump-down showing the 60-foot sphere ambient pressure vs. time is provided in Fig. 4. The sphere High PT is shown from atmospheric pressure to 1.5 kPa, at which point the instrument uncertainty (0.3 kPa) is 20% of the reading. The Low PT is shown from 1.4 kPa to the minimum achieved pressure of approximately 95 Pa. Also shown in Fig. 4 are the time stamps where laser scattering (LS) measurements were acquired during pump-down. A dense fog, which can be attributed to the condensation of moisture in the sphere, was typically observed once pump-down was initiated. This fog usually started to clear near 30 kPa, however the LS instrument was typically able to see scattering from liquid clusters until approximately 20 kPa. As part of pump-down procedures, the steam ejector was isolated near 13 kPa to perform a diagnostics check. The isolation of the steam ejector can be seen in the flat region of the pressure trace in Fig. 4 at approximately 60 minutes. The activation of the facility blowers at approximately 115 minutes can also be seen in Fig. 4, as the pump-down rate increased until a plateau was reached near 145 minutes.

Images acquired using the Rayleigh scattering instrument during pump-down are shown in Fig. 5 for the three ambient pressures (P_a = 13.5 kPa, 969 Pa, and 283 Pa) noted in Fig. 4. These images are shown oriented with respect to the nozzle centerline (r = 0 mm) and the impingement plate (z = 0 mm). The images qualitatively show a decrease in signal intensity as the ambient pressure is reduced. However, quantitative interpretations for the signal intensity with respect to gas density are confounded by the presence of dust particles in the sphere and background laser scattering. This is illustrated in Fig. 6, where z is plotted vs. the signal intensity (averaged over the $-10 \text{ mm} \leq r \leq +10$ mm region. Scattering from the plate surface can be seen near z = 0 mm and from the out-of-focus image of the curvature of the inner plate near z = 17 mm (due to the camera perspective). In between these regions, a qualitative trend of higher signal with greater gas densities (through the greater ambient pressure) is evident, although the signal is very noisy due to the particle scattering.

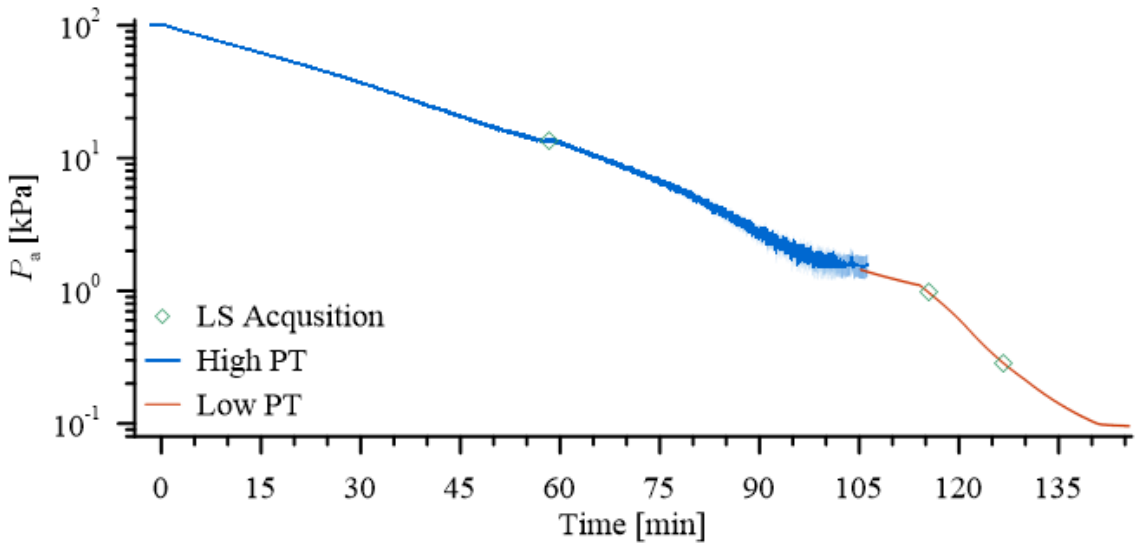
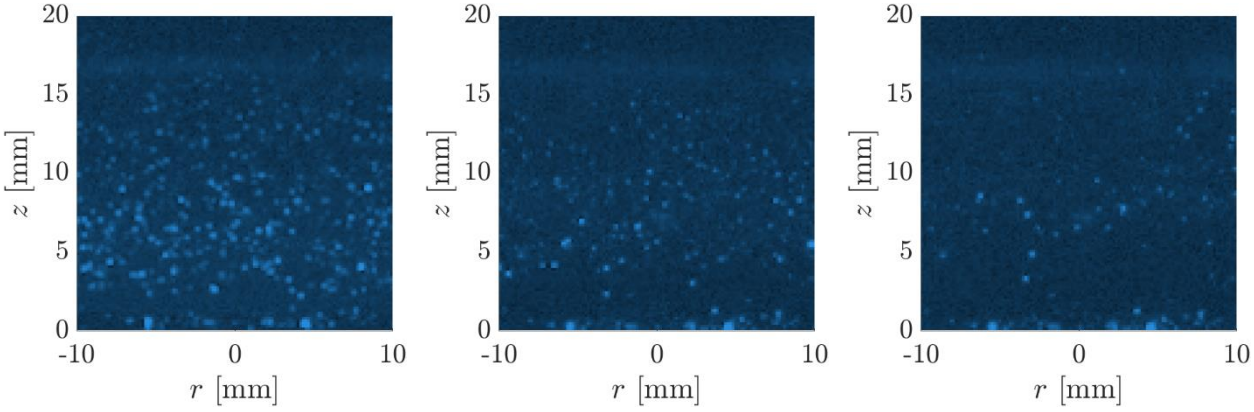


Fig. 4. Representative sphere ambient pressure P_a vs. time during pump-down. The symbols represent timestamps where laser scattering (LS) data was collected.



(a) **(b)** **(c)**

Fig. 5. Time-averaged laser scattering (LS) images obtained during sphere pump-down at: (a) P_a = 13.5 kPa, (b) P_a = 969 Pa, and (c) P_a = 283 Pa. The images correspond to the LS Acquisition points shown in Fig. 4.

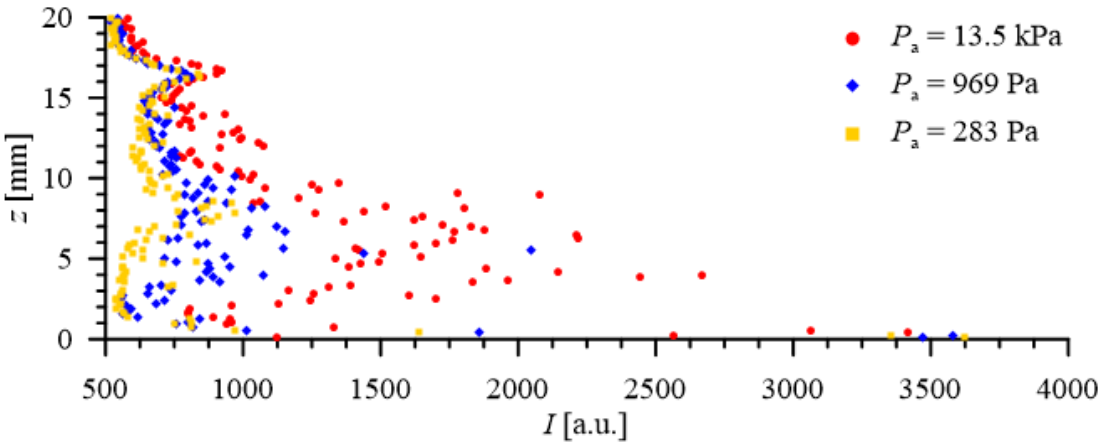


Fig. 6. Vertical axis z vs. scattering intenity I for three different sphere ambient pressures corresponding to the LS Aquisiton points shown in Fig. 4.

B. Plume Flow Parameters

Measured values for the nozzle stagnation pressure and vacuum sphere ambient pressure over the test run are shown in Fig. 7(a) as a function of time. The corresponding figure for the nozzle stagnation temperature and vacuum sphere ambient temperature is shown in Fig. 7(b). In this and subsequent figures, t = 0 s corresponds to the received feedback on the DAQ indicating that the pneumatic valve upstream of the nozzle received its command to open. This is indicated with the dashed vertical line at t = 0 s, while a second dashed vertical line near t = 5.7 s indicates the feedback from the valve that it received the command to close. The pressure transducers located at the nozzle plenum (Nozzle PT #1 and Nozzle PT #2) appear to measure nearly identical values. The stagnation pressure varied from approximately 3900 to 4300 kPa over the test run, with a relatively flat profile of approximately 4000 kPa near t = 4 s. The ambient pressure (as measured by the Sphere Low PT) increased from P_a = 84 Pa at t = 0 s to P_a = 123 Pa at t = 5.7 s. As seen in Fig. 7(b) the stagnation temperature of the ethane, as measured by the Nozzle TC #1 and Nozzle TC #2, was near 293 K at the start of the run. Although the ethane was heated over three different heating stages and nozzle hardware was maintained at an elevated temperature, thermal losses in the flow system resulted in the ethane flow beginning at a relatively low temperature. The greatest rise in the ethane temperature occurred in the first second of flow, with a temperature near 540 K achieved at t = 1 s. The stagnation temperature continued to increase during the rest of the test run and reached 643 K at t = 5.7 s. The ambient temperature in the sphere was constant over the test run at approximately T_a = 283 K. Since the nozzle pressure transducer and thermocouple pairs measured nearly identical values between the dashed lines, the mean of the two readings were used as the plume stagnation pressure P_0 and plume stagnation temperature T_0, respectively.

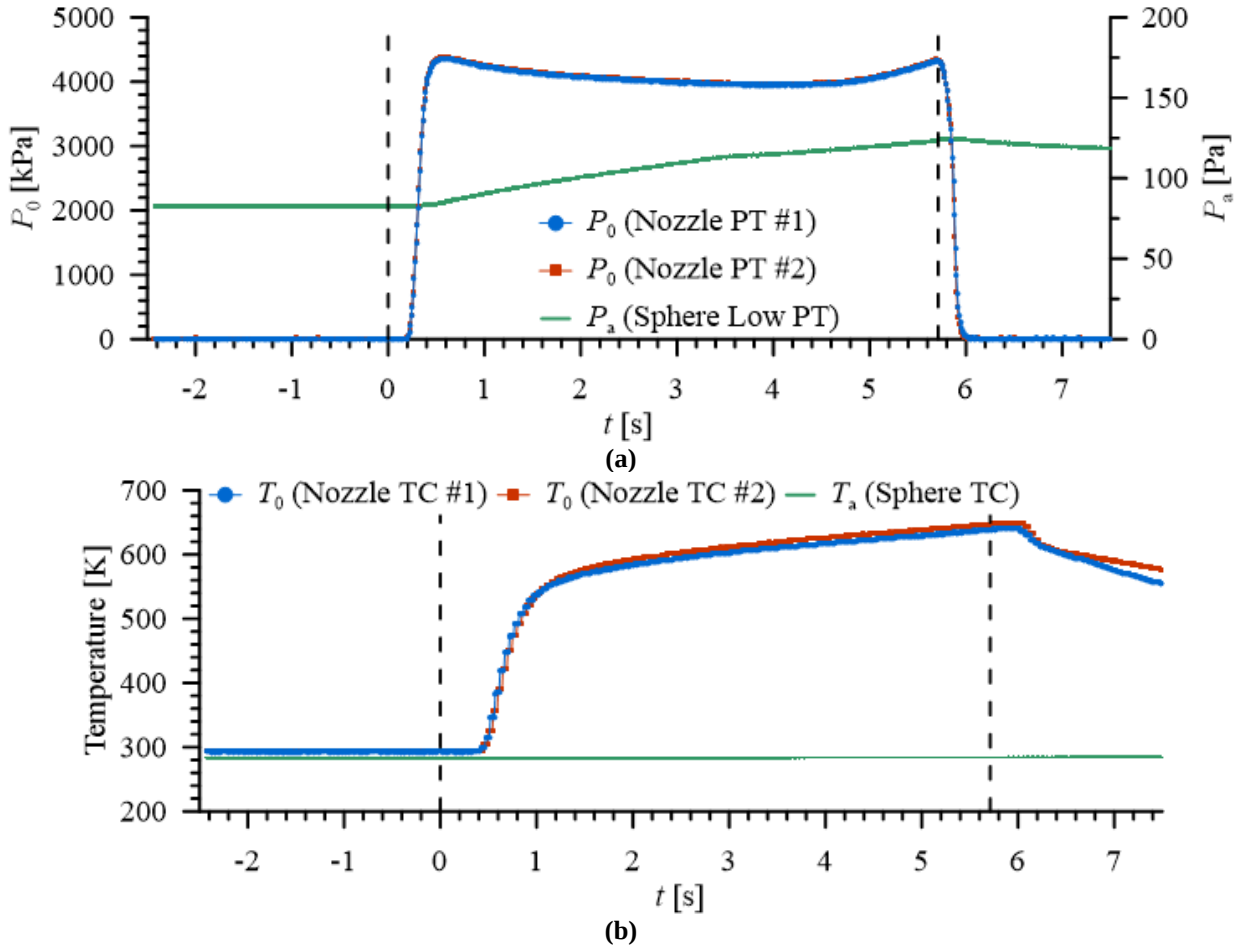


Fig. 7. (a) Nozzle stagnation pressure P_0 and sphere ambient pressure P_a vs. time and (b) nozzle stagnation temperature T_0 and sphere ambient temperature T_a vs. time. Also shown are vertical dashed lines representing received valve feedback indicating the open command near t = 0 s and close command near t = 5.7 s.

A phase diagram of ethane indicating the liquid, gas (superheated), and supercritical phases, and the saturation pressure P_{SAT} as a function of temperature are shown in Fig. 8. The supercritical region corresponds to temperatures and pressures greater than the critical temperature (305 K) and critical pressure (4872 kPa), respectively. Thermodynamic properties were obtained for this figure and throughout this paper with real gas effects included using the program Engineering Equation Solver [37]. Figure 8(a) shows the phase diagram with the plume stagnation temperature and pressure data for the time between the dashed vertical lines in Fig. 7. The phase diagram shows that the majority of the test run occurred with the ethane in the nozzle plenum firmly in the gas phase. However, two-phase flow in the plenum may have been present during the nozzle start-up transient before the rapid temperature increase. The phase diagram with the properties at the nozzle exit for the test run after t = 0.75 s are shown in Fig. 8(b). For early test times, the calculated phase at the nozzle exit indicates a two-phase flow. However, due to the relatively short timescales from the nozzle plenum to exit, two-phase flow may not necessarily have been present at the nozzle exit. For data points yielding a gaseous nozzle exit condition, exit properties were determined by calculating the exit specific heat ratio γ_e, exit Mach number M_e, exit Temperature T_e, and exit Pressure P_e through simultaneously solving equations 2 – 5:

$$\gamma_e = \frac{c_p(T_e, P_e)}{c_v(T_e, P_e)}, \tag{2}$$

$$\frac{A_e}{A_t} = \left(\frac{\gamma_e+1}{2}\right)^{-\frac{\gamma_e+1}{2(\gamma_e-1)}} \frac{\left(1+\frac{\gamma_e-1}{2}M_e^2\right)^{\frac{\gamma_e+1}{2(\gamma_e-1)}}}{M_e}, \tag{3}$$

$$\frac{T_e}{T_0} = \left(1+\frac{\gamma_e-1}{2}M_e^2\right)^{-1}, \tag{4}$$

$$\frac{P_e}{P_0} = \left(1+\frac{\gamma_e-1}{2}M_e^2\right)^{-\frac{\gamma_e}{\gamma_e-1}}. \tag{5}$$

As discussed in Ref. 29, the specific heat ratio of ethane is sensitive to temperature. As a result, the nozzle exit Mach number would slightly vary during the test run due to changes in temperature. Both γ_e and M_e are shown in Fig. 9(a) vs. time for the 0.75 s ≤ t ≤ 5.71 s range (time in-between dashed lines in Fig. 7). It can be seen that the exit Mach number decreased from M_e = 3.50 at t = 0.75 to M_e = 3.18 at t = 5.71 due to the change in the exit specific heat ratio from γ_e = 1.27 at t = 0.75 to γ_e = 1.17 at t = 5.71. Derived plume properties were likewise affected and the corresponding exit pressure ratio P_e/P_a and exit Reynolds number Re_e are shown as a function of test time in Fig. 9(b). A 2-second window where these two parameters were relatively constant occured within 3.50 ≤ t ≤ 5.50, indicated with solid vertical lines in Fig. 9(b). Rayleigh scattering data of ethane within this time period are discussed in the next section. Key plume parameters during the steady-state period are summarized in Table 2.

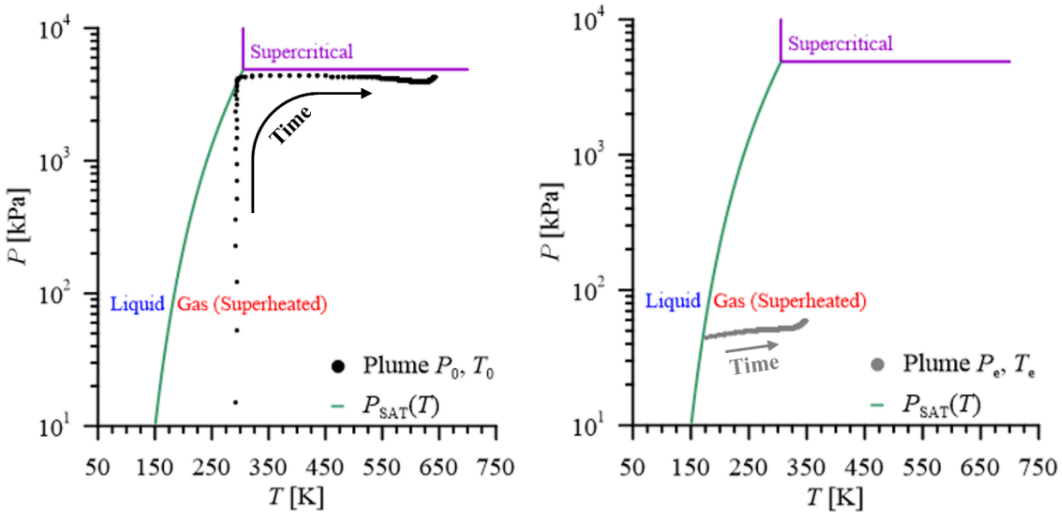


Fig. 8. Phase diagram of ethane with (a) measured at nozzle plenum and (b) calculated at nozzle exit.

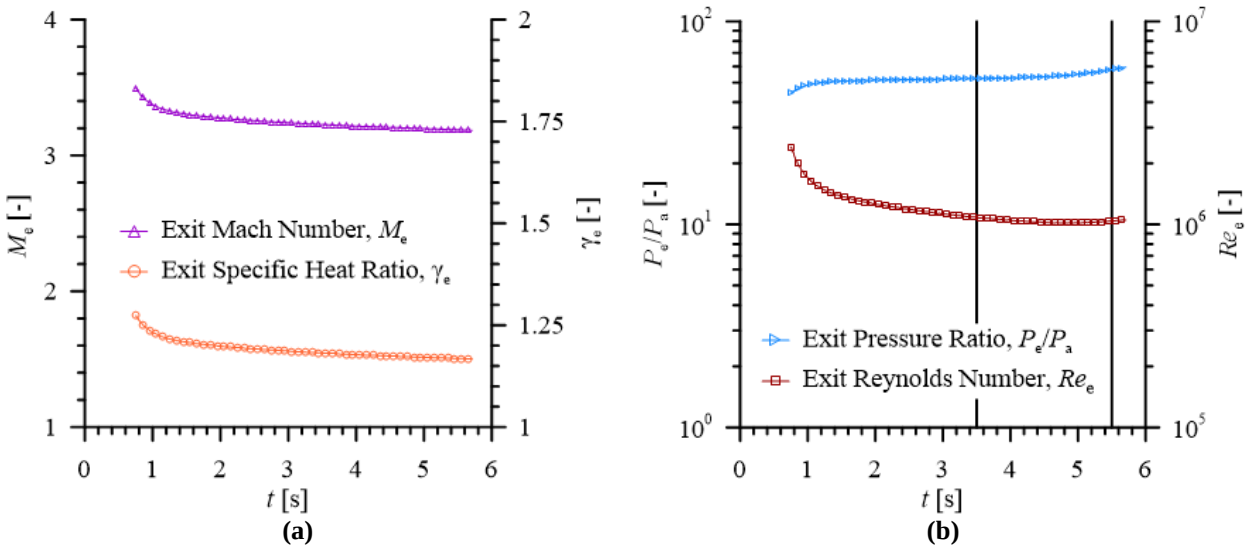


Fig. 9. Nozzle exit parameters vs. time: (a) Mach number and specific heat ratio and (b) pressure ratio and Reynolds number. The solid vertical lines in (b) indicate the 2 seconds used for steady-state derived quantities.

Table. 2. Mean and standard deviation values for key parameters during 3.50 s ≤ *t* ≤ 5.50 s.

	[K]	[kPa]	[Pa]	[-]	[-]	[-]
	T_0	P_0	P_a	M_e	P_e/P_a	Re_e
Mean	628	4016	117	3.21	464	$1.04 \cdot 10^6$
Standard Deviation	7	79	3	0.01	6	$0.02 \cdot 10^6$

C. Stagnation Shock Imaging

Instantaneous laser Rayleigh scattering images of the supersonic plume impingement are shown in Fig. 10 during the 3.50 s ≤ *t* ≤ 5.50 s period. Although data was acquired at 10 Hz, the images are shown here at 2 Hz (or every 0.5 seconds) to illustrate general trends. The curved stagnation shock, appearing concave and facing upwards, is distinguishable in each of these images within the -80 mm ≤ *r* ≤ 80 mm region. Lower gas density regions beyond *r* = ±80 mm reduce the image contrast. Also apparent is the presence of particulates of unknown origin, appearing as bright Mie scattering from particles and even ligament-like structures, such as those in Fig. 10(b). Further investigation is currently underway to determine if the particulates are condensed ethane droplets, contaminants in the flow system, an artifact of paint fragments from impingement on the plate surface, or related to another phenomena not yet identified. The stagnation shock position does not appear to vary with time for the nearly constant plume properties within 3.50 s ≤ *t* ≤ 5.50 s. Therefore, steady, laminar behavior is believed to be present for the plume impingement near the centerline. Unsteady behavior may be present, however, near the plume shear layer and for the resultant wall-jet.

The steady stagnation shock behavior allows the possibility of filtering the particulates from the sequence of images, as particle scattering would appear as outliers. An outlier removal based on the median absolute deviation was performed using the signal intensity vs. time data on a pixel-to-pixel basis for the 21 images acquired during 3.50 s ≤ *t* ≤ 5.50 s. The laser scattering signal intensity vs. time for two centerline (*r* = 0 mm) positions corresponding to before (*z* = 5 mm) and after (*z* = 7 mm) the stagnation shock is shown in Fig. 11. The open symbols in this figure indicate the detected outliers, which are more than three median absolute deviations from the median. The processed ensemble image showing the mean signal intensity after the outlier removal is shown in Fig. 12(a). Some artifacts from the particle scattering are still present in the image and the artifacts from geometric scattering on the surface are also apparent. Nevertheless, significant improvements in terms of the stagnation shock visualization are apparent in the ensemble image compared to the instantaneous images in Fig. 10. The height of the stagnation shock as a function of the radial location was extracted using a semi-automatic custom edge detection algorithm and is shown in Fig. 12(b), along with a 2nd order polynomial (quadratic) fit. The height of the stagnation shock at *r* = 0 mm was measured to be z_{SS} = 6.15 mm based on the ensemble image. The same value for the stagnation shock height was also obtained

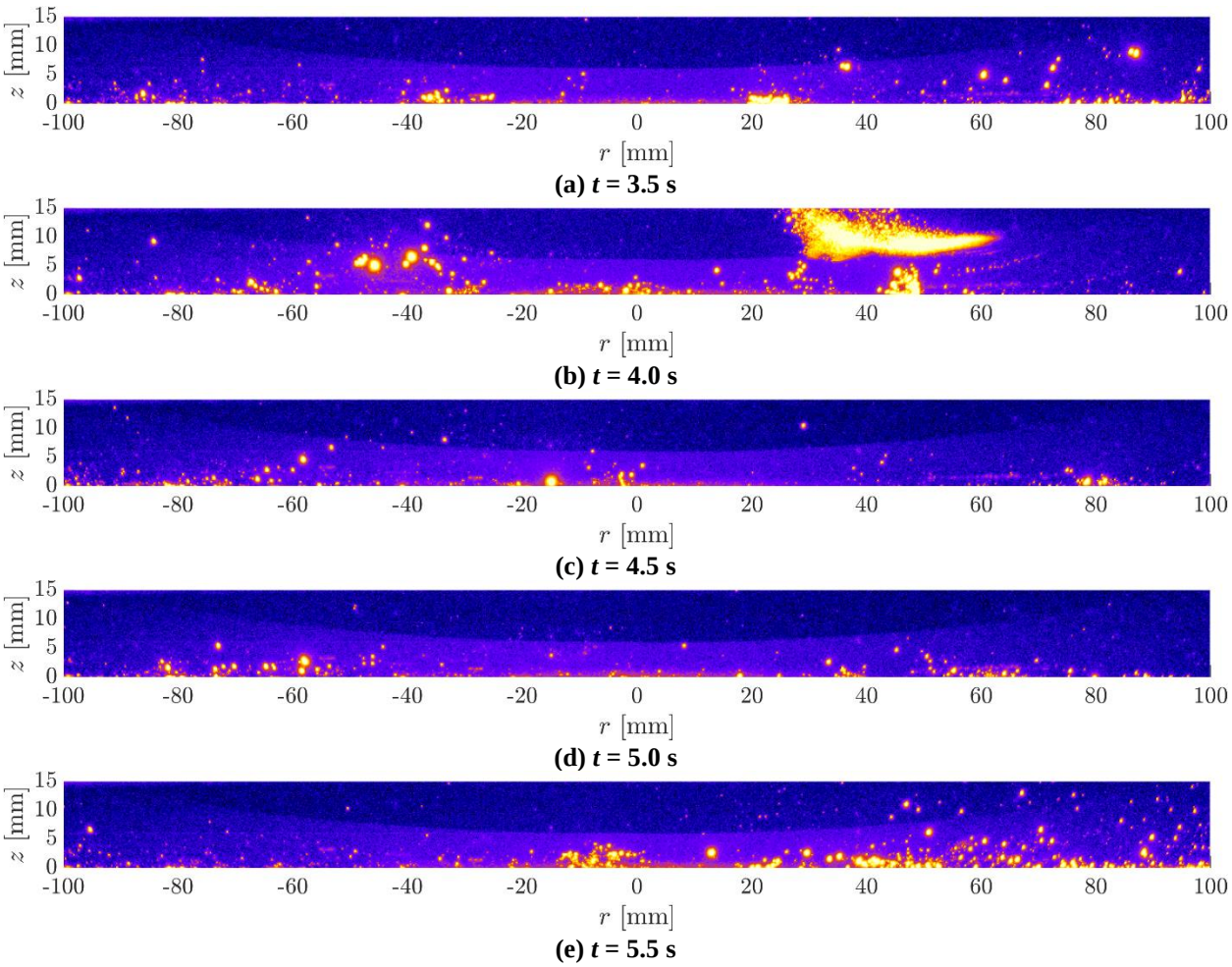


Fig. 10. Instantaneous laser scattering images acquired during the test run at parameters corresponding to nearly steady-state operation at approximately P_e/P_a = 464 and Re_e = 1.04·10^6. The stagnation shock is clearly visible due to the sharp change in gas density across the shock; however, geometric scattering is also evident.

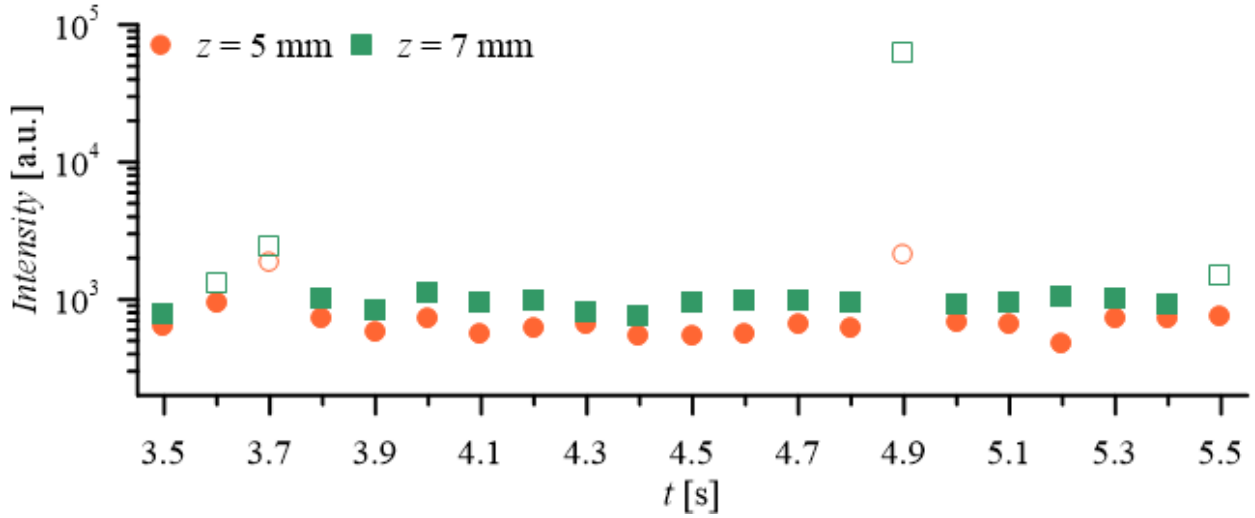


Fig. 11. Laser scattering intensity vs. time (during 3.5 s ≤ t ≤ 5.5 s) for two centerline (r = 0 mm) positions before (z = 5 mm) and after (z = 7 mm) the stagnation shock; open symbols indicate detected outliers.

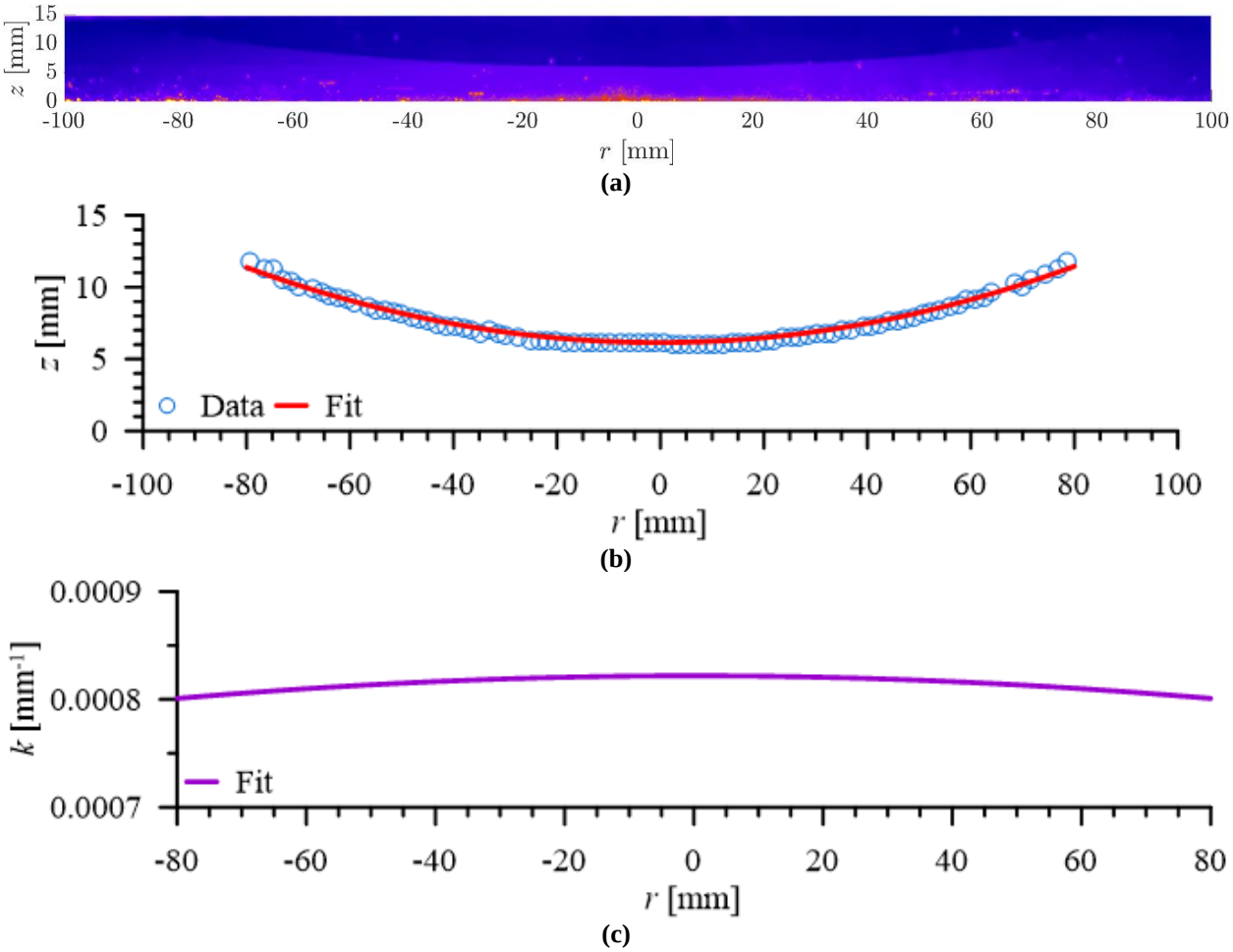


Fig. 12. (a) Processed ensemble laser Rayleigh scattering image (during 3.5 s ≤ t ≤ 5.5 s). The stagnation shock location identified through edge detection is shown in (b) with a polynomial fit. The calculated curvature from the polynomial fit is shown in (c).

from the instantaneous images after performing the outlier removal and averaging over the -10 mm ≤ r ≤ 10 mm region. Averaging over this region was performed since the height of the stagnation shock appears to be nearly constant within these radial locations near the centerline based on the ensemble image. The quadratic fit shown in Fig. 12(b) can be used for validation of numerical solutions of the plume impingement behavior and is provided in Eq. 6:

$$z_{SS}(r) = ar^2 + br + c$$
$$a = 8.22 \cdot 10^{-4}\ \text{mm}^{-1};\ b = 4.81 \cdot 10^{-4}\ \text{mm}^{0};\ c = 6.15\ \text{mm}. \quad (6)$$

The curvature of the stagnation shock k_{SS} as a function of r for the quadratic fit is shown in Fig. 12(c) and was calculated using the expression provided in Eq. 7:

$$k_{SS} = \frac{2a}{(1 + (2ar + b)^2)^{3/2}}. \quad (7)$$

The height of the stagnation shock, normalized by the exit diameter, from the data reported in this paper is compared with the values in the literature from Rodrigues *et al.* [25]. The stagnation shock height comparison is shown in Fig. 13 as a function of P_e/P_a. The stagnation shock height reported in this paper is much closer to the surface than the literature values. Futhermore, this does not appear to primarily be an effect of the exit Reynolds number, as the values from Ref. 25 are relatively insenstive to Re_e. Although the data from Rodrigues *et al.* shown in Fig. 13 were obtained at $h/D_e = 10$, compared to $h/D_e = 8$ for the present work, the images of the stagnation shock from both experiments

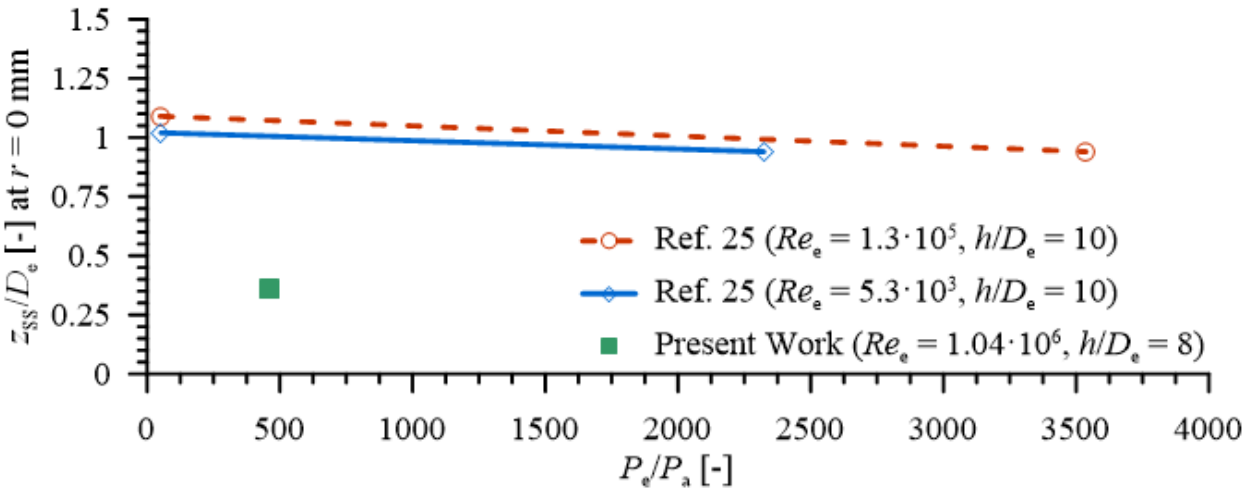


Fig. 13. Dimensionless stagnation shock height z_{SS}/D_e vs. jet pressure ratio P_e/P_a for the present work and the data reported by Rodrigues *et al.* [25].

show a similar qualitative behavior in terms of their concave shape. Further experimental efforts are therefore needed to elucidate the sensitivity of the stagnation shock height to the plume impingement parameters.

V. Summary and Conclusions

This paper describes a plume impingement experiment performed at the NASA Langley 60-foot vacuum sphere involving an inert, non-combusting ethane plume and a flat plate. The gas-phase nature of this work, i.e. impingement on a flat plate, focuses on initial characterization efforts of the supersonic plume impingement and is primarily driven to verify that the expected plume flowfield is obtained prior to testing with lunar regolith simulant. Laser Rayleigh scattering was performed at the impingement plate, enabling visualization of the stagnation shock and extraction of the stagnation shock height. This paper marks the first use of a laser-based measurement technique at this large-scale, legacy NASA facility. Efforts are underway to continue investigation of the plume impingement behavior and testing with lunar regolith simulant is planned for the near future. The integration of a high-power, pulsed laser system at this facility also aids the future use of more sophisticated diagnostics such as particle imaging velocimetry and planar laser-induced fluorescence.

Acknowledgments

The authors wish to acknowledge the support of the NASA Exploration Systems Development Mission Directorate (ESDMD) Human Landing Systems (HLS) program for support of the entire HLS PSI Ground Test efforts and the Space Technology Mission Directorate (STMD) Plume Surface Interaction Instrumentation (PSII) project for support with hardening of the machine vision cameras. Several engineers and technicians were involved with test design, integration, and execution at the 60-foot sphere, including invaluable contributions from: D. Jones and Dr. N. Nugent at NASA Stennis Space Center; W. Joyner, S. Barnett, S. Parks, D. Cole, C. Good, C. Eshleman, O. Tyrrell, J. Ortiz, B. Russ, A. Jackson, J. Allen, H. Gotaire, J. Engelhardt at NASA Langley Research Center, Dr. R. Gejji from Purdue University, and N. Smith from IN Space LLC. N. S. Rodrigues thanks Dr. A. Neal Watkins for use of the Quantel Evergreen 200 laser.

References

[1] Cuesta, C. J., Davies, J., Worrall, K., Cammarano, A., and Zare-Behtash, H., "Plume-surface interactions: A review of experimental work," Acta Astronautica 226, 2025. doi: 10.1016/j.actaastro.2024.09.021.

[2] Korzun, A. M., Eberhart, C. J., West, J., Liever, P., Weaver, A., Mantovani, J., Langton, A., Kemmerer, B., and Atkins, A. "Design of a Subscale, Inert Gas Test for Plume-Surface Interactions in a Reduced Pressure Environment," AIAA 2022-1808. *AIAA SCITECH 2022 Forum*. January 2022. doi: 10.2514/6.2022-1808.

[3] Eberhart, C. J., West, J., and Korzun, A. M., "Overview of Plume-Surface Interaction Data from Subscale Inert Gas Testing at NASA MSFC Test Stand 300 Vacuum Facilities," AIAA 2022-1810. *AIAA SCITECH 2022 Forum*. January 2022. doi: 10.2514/6.2022-1811.

[4] Diaz-Lopez, M. X., Gorman, M., Rubio, J. S., and Ni, R., "Plume-surface Interaction Physics Focused Ground Test 1: Diagnostics and Preliminary Results," AIAA 2022-1809. *AIAA SCITECH 2022 Forum*. January 2022. doi: 10.2514/6.2022-1810.
[5] Rubio, J. S., Gorman, M., Diaz-Lopez, M. X., and Ni, R., "Plume-Surface Interaction Physics Focused Ground Test 1: Setup and Preliminary Results," AIAA 2022-1809. *AIAA SCITECH 2022 Forum*. January 2022. doi: doi.org/10.2514/6.2022-1809.
[6] Gorman, M. T., Rubio, J. S., Diaz-Lopez, M. X., Chambers, W. A., Korzun, A. M., Rabinovitch, J., and Ni, R., "Non-intrusive, 3D Optical Measurements of Crater Formation due to Plume-Surface Interactions," PNAS nexus 2(9), 2023. doi: 10.1093/pnasnexus/pgad300.
[7] Rubio, J. S., Rodrigues, N. S., Qi, Y., Diaz-Lopez, M. X., Gorman, M. T., and Ni, R., "On the Interaction Between a Flow Instability and Inertial Particles in Supersonic Jet Plume-Surface Interaction," AIAA 2025-2567. *AIAA SCITECH 2025 Forum*. January 2025. doi: 10.2514/6.2025-2567.
[8] Rubio, J. S., Rodrigues, N. S., Qi, Y., Patel, M., Gorman, M. T., Diaz-Lopez, M. X., Capecelatro, J., Danehy, P. M., and Ni, R., "Dusty streaks on the Moon: fingerprints of multiphase flow instabilities," *Nature Communications* 16:6670, 2025. doi: 10.1038/s41467-025-62001-8.
[9] Stubbs, D., Silwal, L., Thurow, B. S., Hirabayashi, M., Raghav, V., and Scarboroughand, D., "Three-Dimensional Measurement of the Crater Formation During Plume–Surface Interactions Using Stereo-Photogrammetry," AIAA Journal 60(3), 2022. doi: 10.2514/1.J060835.
[10] Stubbs, D., Silwal, L., Bhargav, V. , Thurow, B. S., Hirabayashi, M., Raghav, V., and Scarboroughand, D., "Non-intrusive, 3-D Crater Formation Measurements Due to Plume-Surface Interactions Under Sub-Atmospheric Pressure Conditions," AIAA 2023-2488. *AIAA SCITECH 2023 Forum*. January 2023. doi: 10.2514/6.2023-2488.
[11] Bhargav, V. N., Silwal, L., Stubbs, D., Fulone, B. K., Thurow, B. S., Scarboroughand, D., and Raghav, V., "Characterization of Ejecta Sheet Generated by Jet-Impulse During Plume-Surface Interactions," AIAA 2024-2526. *AIAA SCITECH 2024 Forum*. January 2024. doi: 10.2514/6.2024-2526.
[12] Silwal, L., Bhargav, V. N., Stubbs, D. C., Fulone, B. K., Thurow, B. S., Scarboroughand, D., and Raghav, V., "Ejecta behavior during plume-surface interactions under rarefied atmospheric conditions," Acta Astronautica 218, 2024. doi: 10.1016/j.actaastro.2024.02.013.
[13] Stubbs, D., Silwal, L., Bhargav, V. N., Thurow, B. S., Raghav, V., and Scarboroughand, D., "The Effect of Reduced Ambient Pressure on Plume-Surface Interaction Cratering Dynamics," AIAA Journal 63(3), 2025. doi: 10.2514/1.J064431.
[14] Subramanian, S., Wilson, A., White, C., Kontis, K., Evans, D., and Van den Eynde, J., "Tracking plume-regolith interactions in near-vacuum conditions," *Physics of Fluids* 36:1, 2024. doi: 10.1063/5.0180669.
[15] Ukai, T., Subramanian, S., Wilson, A., Craig, B., Kontis, K., "Initial particle ejection behaviours due to a hypersonic jet impingement at different high-nozzle pressure ratios in rarefied atmospheric conditions," *Acta* Astronautica 222, 2024. doi: 10.1016/j.actaastro.2024.06.009.
[16] Subramanian, S., Wilson, A., White, C., and Kontis, K., "Crater formation and particle ejection induced by supersonic jet impingement in near-vacuum," *Acta* Astronautica 232, 2024. doi: 10.1016/j.actaastro.2025.03.017.
[17] Subramanian, S., White, C., Kontis, K., Evans, D. and Van den Eynde, J., "Experimental Study of Plume surface interaction in the Martian Environment," AIAA 2025-0516. *AIAA SCITECH 2025 Forum*. January 2025. doi: 10.2514/6.2025-0516.
[18] Rasmont, N., Al-Rashdan, H., Elliott, G. S., Rovey, J., and Villafane-Roca, L., "Spatially Distributed Measurements of Ejecta Concentrations in Plume-Surface Interactions using Millimeter Wave Interferometry," AIAA 2023-0465. *AIAA SCITECH 2023 Forum*. January 2023. doi: 10.2514/6.2023-0465.
[19] Rasmont, N., Bansal, I., Al-Rashdan, H., Elliott, G. S., Rovey, J., and Villafane-Roca, L., "Millimeter-Wave Tomographic Interferometry of Ejecta Concentrations in Plume-Surface Interactions," AIAA 2024-1979. *AIAA SCITECH 2024 Forum*. January 2024. doi: 10.2514/6.2024-1979.
[20] Rasmont, N., Heuser, L., Rovey, J., and Villafane-Roca, L, "Multiple Approach for Ejecta Mapping in PSI: Millimeter-Wave Tomography Coupled with PTV and Predictive Modeling," AIAA 2025-2400. *AIAA SCITECH 2025 Forum*. January 2025. doi: 10.2514/6.2025-2400.
[21] Vick, A. R. and Andrews Jr., E. H., "An investigation of highly underexpanded exhaust plumes impinging upon a perpendicular flat surface," Technical Note NASA/TN D-3269, 1966.
[22] Al-Rashdan, H., Rasmont, N., Rovey, J., Elliott, G., and Villafane-Roca, L., "Static wall pressure measurements of supersonic underexpanded jet impingement," AIAA 2021-2859, 2021. doi: 10.2514/6.2021-2859.
[23] Subramanian, S., Craig, B., White, C., Kontis, K., Evans, D., and Van den Eynde, J., "Underexpanded jet impingement in near vacuum environment," *Physics of Fluids* 36:107104, 2024. doi: 10.1063/5.0230314.
[24] Rodrigues, N. S., Tyrrell, O. K., and Danehy, P. M., "Fluorescence imaging of plume-surface interaction in large-scale reduced pressure environments," *Physics of Fluids* 36:10, 2024. doi: 10.1063/5.0223210.
[25] Rodrigues, N. S., Tyrrell, O. K., Danehy, P. M., Eberhart, C. J., McDougal, K. J., Liu, T., Reynolds, T. D., Rubio, J. S., Jiang, N., Hsu, P., and Korzun, A. M., "Flow Visualization for Plume-Surface Interaction Testing Within Large-Scale Vacuum Environments at Conditions Relevant to Lunar and Martian Landers", *JANNAF Exhaust Plume and Signatures Annual Meeting*. December 2023.
[26] Tyrrell, O. K., Rodrigues, N. S., Korzun, A. M., and Danehy, P. M., "Flow visualization of intrusive and non-intrusive configurations for lunar- and Martian-relevant plume-surface interaction," AIAA 2024-2499. *AIAA SCITECH 2024 Forum*. January 2024. doi: 10.2514/6.2024-2499.

[27] Plume-Surface Interaction at Martian-relevant Lander Environments," AIAA 2024-4914. *AIAA ASCEND 2024 Forum*. July 2024. doi: 10.2514/6.2024-4914.
[28] Rodrigues, N. S., Burns, R. A., Tyrrell, O. K., and Danehy, P. M., "Wall-jet evolution during plume-surface interaction using PLIF imaging," AIAA 2025-2402. *AIAA SCITECH 2025 Forum*. January 2025. doi: 10.2514/6.2025-2402.
[29] Inman, J. A., Danehy, P. M., Nowak, R. J., and Alderfer, D. W., "Fluorescence imaging study of impinging underexpanded jets," AIAA 2008-619. 46th AIAA Aerospace Sciences Meeting and Exhibit. January 2008. doi: 10.2514/6.2008-619.
[30] Jones, D. R., "Physical Simulation of Rocket Exhaust Aerodynamics Using Heated Ethane: Conceptual Foundations," NASA TM-2019-220446, 2019.
[31] Jones, D. R., "Physical Simulation Of Rocket Exhaust Aerodynamics Using Heated Ethane: Prototypical Experiments," NASA TM-2020-5009122, 2020.
[32] Miles, R. B., Lempert, W. R., and Forkey, J. N., "Laser Rayleigh scattering," *Measurement Science and Technology* 12, 2001. doi: 10.1088/0957-0233/12/5/201.
[33] Eckbreth, A. C., Laser Diagnostics for Combustion Temperature and Species, 1st ed., CRC Press, London, 1996, Chap. 5.
[34] Land, N. S. and Scholl, H. F., "Scaled Lunar Module Jet Erosion Experiments," NASA TN D-5051, 1969.
[35] Clark, L. V., "Effect of retrorocket cant angle on ground erosion – a scaled Viking study," NASA TM X-2075, 1970.
[36] Klein, S.A., EES – Engineering Equation Solver, Ver. 11.808, F-Chart Software, 2024.